Chapter

Synthesis, Properties, and Characterization of Field's Alloy Nanoparticles and Its Slurry

Chaoming Wang, Xinran Zhang, Wenbing Jia, Wei Wu and Louis Chow

Abstract

This chapter describes a facile one-step method developed for the synthesis of Field's alloy nanoparticles using a nanoemulsification technique and their dispersed them in a base fluid to make slurry. The composition, size, morphology, and thermal properties of as-prepared nanoparticles were characterized by XRF, TEM and, DSC, respectively. The slurry with Field's alloy nanoparticles exhibited good thermal properties and stability. Meanwhile, an experimental study was performed to investigate the jet impingement of HFE7100 fluid with nanosized metallic (Field's alloy) phase change materials (nano-PCM). Surface modification was used to stabilize the slurry of the nano-PCM in HFE7100 fluid and make the slurry stable for over 1 month. The Field's alloy nano-PCM absorbed heat during a phase change process from solid to liquid phase coupled with HFE7100 evaporation process. The effects of mass fraction of Field's alloy nano-PCM on the pressure drop and heat transfer performances of the slurry were investigated through a heat transfer loop test. Away from the critical heat flux, Field's alloy nano-PCM slurry provided a significant heat transfer enhancement due to the increase in the thermal capacity of the carrier fluid. Moreover, the nano-PCM slurries were able to maintain 97% of their heat removal capability after 5000 thermal cycles.

Keywords: Field's alloy, nanoparticles, nanoemulsification, slurry, HFE7100, jet impingement heat transfer

1. Introduction

With their wide industrial and civil applications, heat transfer fluids (HTFs) have been potentially used in lubrication, energy storage, heat exchange, electronic cooling, and so on [1–5]. However, for conventional HTFs (such as water, polyalphaolefin (PAO), fluorocarbons, and glycols), the main drawback of deficient heat transfer performance owing to their low thermal conductivities has limited their practical applications. For the purpose of improving their heat transfer properties, earlier research efforts have been carried out by dispersing those materials, which have high thermal conductivities, such as silver, copper, alumina, copper oxide, silicon carbide, and carbon nanotubes, into HTFs [6–12].

Until recently, adding nano-sized phase change materials (nano-PCMs) into base HTFs attracts considerable attentions. The most frequently used PCMs include

inorganic PCMs, such as metal, alloy and salt hydrates, and organic PCMs, such as paraffins, polyethylene glycols, fatty acids, and esters [13–19]. Different types of nano-PCMs can be synthesized by using various synthetic methods [20–22]. By encapsulating or coating the nano-PCM with a suitable layer, the nano-PCMs can be dispersed in a base fluidic phase. However, nano-sized particles have a strong tendency to agglomerate and easily lead to precipitate in HTFs, which restricts their application as thermal energy storage media. Therefore, encapsulation or surface modification of nanoparticles to increase their dispersion ability in the carrier fluid is of primary importance. Various techniques such as interface polymerization [23] and coacervation [24] and emulsion polymerization [25, 26] were explored to make encapsulated nano-PCM. Meanwhile, some modified nanoparticles using certain way exhibit excellent dispersion stability in some HTFs [27–29]. As inexpensive and stable dielectric HTFs, PAO and HFE7100 are usually applied in cooling of avionic systems [30, 31].

Among those PCMs, the thermal conductivity of lots of low melting point metals, such as indium (In), bismuth (Bi), tin (Sn), and lead (Pb) and their eutectics, is at least two orders higher than that of inorganic PCMs. Meanwhile, their latent heat density and other thermal properties are comparable to inorganic PCMs, which makes low melting point metals or eutectic alloys highly attractive PCMs in practical applications. By taking advantages of nano-PCMs (such as their small size, large surface-to-volume ratio, good dispersion ability in base fluid, and large latent heat of fusion), these HTFs have some distinct merits such as high energy density thermal storage, large specific heat capacity, low flow drag, and enhanced thermal conductivity. Meanwhile, the fluids still keep the fluidic properties. All these aforementioned merits make these thermal fluids containing nano-PCM a promising HTF for electronic cooling equipment, thermal control, and those systems requiring high heat transfer rates [32–34]. The tight contact of nanoparticle and base fluid decreases the heat transfer resistance between nanoparticles and fluid, thus enabling fast exchange of heat transfer between phases [35]. Therefore, the slurry with nano-PCM could decrease the total pumping power in a heat transfer loop due to the increased heat capacity of the carrier fluid.

For a liquid, when the flow rate and thermal conductivity keep constant, the heat transfer capability is predominantly depending on its heat absorbing capacity [36]. Frequently, in high-flux heat removal case, dielectric fluids (such as HFE7100) are usually used to take the heat away through utilizing their latent heat of vaporization. As a low melting point alloy, Field's alloy is a eutectic alloy melt at approximately 62°C (144 F), in which composes with the weight percentage of 32.5% bismuth (Bi), 51% indium (In), and 16.5% tin (Sn). As a low melting point alloy, Field's alloy is selected due to its melting temperature a litter higher than the boiling point of HFE7100. Therefore, during liquid-vapor phase transition of HFE7100, the thermal fluid heat capacity can be increased significantly when the nano-PCM changes from the solid to liquid phase.

This chapter mainly summarized our works in recently few years [37, 38], which include: (1) synthesis and modification of Field's alloy nanoparticles; (2) characterization of as-prepared Field's alloy nanoparticles; (3) jet impingement heat transfer of Field's alloy nanoparticles-HFE7100 slurry.

2. Synthesis and modification of Field's alloy nanoparticles

Nanoemulsification method is one of the most facile techniques to prepare nano-sized Field's alloy particles. The illustrated nanoemulsification formation process is shown in **Figure 1**. Briefly, a certain amount of Field's alloy pellets was put into PAO

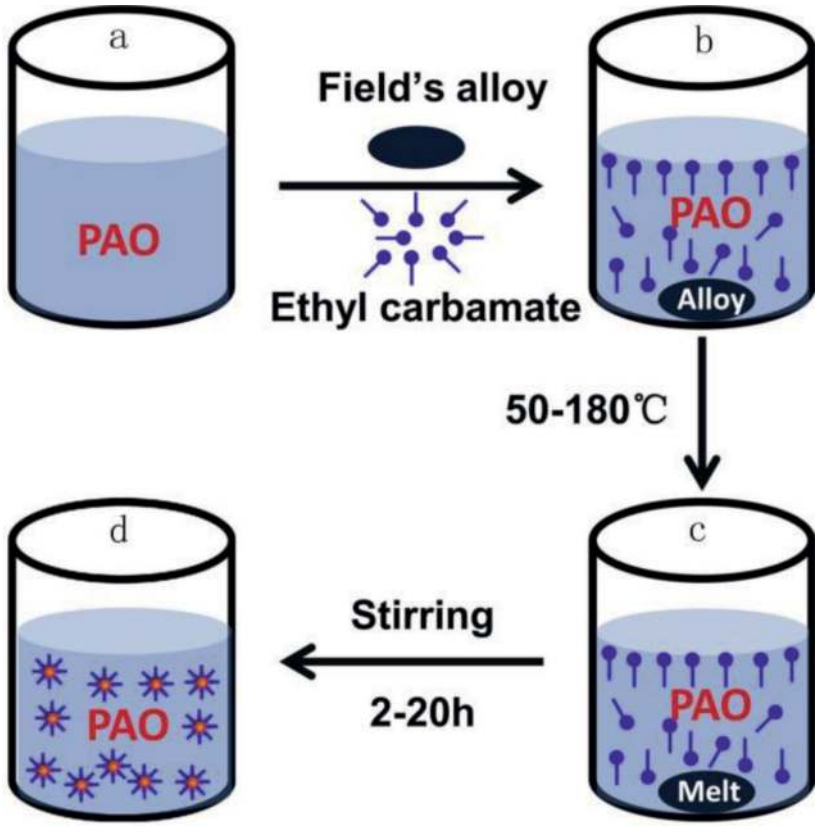

Figure 1.
Illustrated scheme of the synthesis of molten Field's alloy nanoparticles using nanoemulsification method. (a) PAO and molten Field's alloys are in the reaction vessel. These two liquids are immiscible and phase separate; (b) polymer surfactant (ethyl carbamate) is soluble in PAO; (c) the mixture is heated up to certain temperature and the bulk molten alloy formed; (d) the microscale emulsion is stirred and breaks into microscale droplets until nanoemulsion is formed.

oil with or without certain amount of ethyl carbamate as surfactant. After that, the mixture was heated and kept at certain temperature (50, 70, 100, 150, and 180°C) in the help of silicone oil thermal bath and stirring for specific time under certain temperature under nitrogen protection to make the native or ethyl carbamate modified low melting temperature Field's alloy nanoparticles. As the time increases, the white color of PAO oil became gray and dark gradually. When the reaction finished, the nanoparticles were gathered by centrifuge and washed with acetone at least three times and then dried at 45°C overnight for ready to use. The native or modified Field's alloy slurry was made by dispersing certain amount of native or ethyl carbamate modified Field's nanoparticles into the desired base fluid.

In order to make the as-prepared Field's alloy nanoparticles dispersed well in HFE7100 for long time, the nanoparticle surfaces were modified with a monolayer of 1H, 1H, 2H, 2H-perfluorooctyltriethoxysilane by mixing the nanoparticles in a silane solution of HFE7100.

3. Characterization of as-prepared Field's alloy nanoparticles

The size, morphologies, composition, and thermal properties of the synthesized Field's alloy nanoparticles were characterized by transmission electron microscopy (TEM), X-ray fluorescence spectrometry (XRF), and differential scanning calorimetry (DSC). The result and discussions were as the following.

3.1 Size and morphologies of Field's alloy nanoparticles

The size and morphologies of synthesized Field's alloy nanoparticles using nanoemulsion method were investigated by TEM. **Figure 2** showed the TEM images of the as-prepared Field's alloy particles after boiling the Field's alloy pellets in PAO at 180°C for 10 min (**Figure 2A**) and 2 h (**Figure 2B**), respectively. When the boiling time increases, the size of particles would decrease and became more and more spherical. After 10 min, the particles have irregular shapes and with the size range from 200 to 500 nm. As the time increases to 2 hours, the particles showed spherical shapes with the size of about 20 nm. **Figure 2C** showed the plot of reaction time versus the size of particles. After 2 hours, even though the reaction time increase (such as 5, 10, or even 20 h), the particles size did not have too much change, which was still close to 20 nm.

3.2 Composition and thermal properties of Field's alloy nanoparticles

The composition of bulk Field's alloy pellet and the synthesized Field's alloy nanoparticles was deduced with XRF spectrum, which was measured and collected from a mini-X system that uses a mini X-ray tube (Amptek, 40 kV, 100 μA) and a solid state X-ray spectrometer detector (Amptek 123, reflection mode). The whole setup was enclosed in a lead containing acrylic chamber with 1 mm of lead equivalent thickness to make sure no X-ray comes out. As shown in **Figure 3A**, no obvious difference is observed between the composition of the bulk Field's alloy materials and the as-prepared nanoparticles, in which $L_{\alpha 1}$, $K_{\alpha 1}$, and $K_{\alpha 2}$ of indium at 3.29,

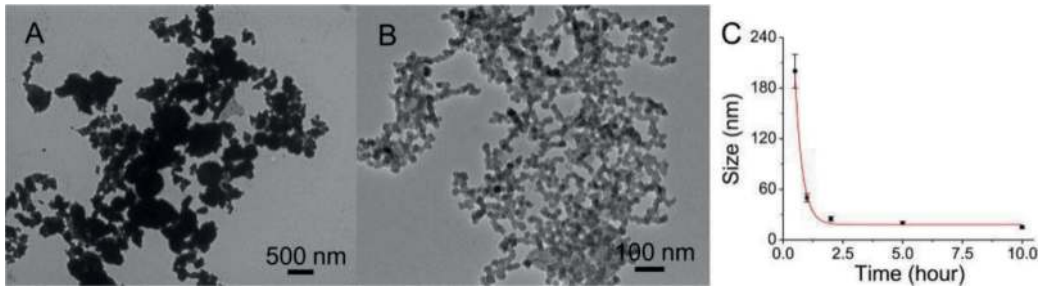

Figure 2.
TEM images of Field's alloy particles synthesized at 180°C for 10 min (A) and 2 h (B) using nanoemulsification method; Field's alloy particles size versus reaction temperature for 2 h (C).

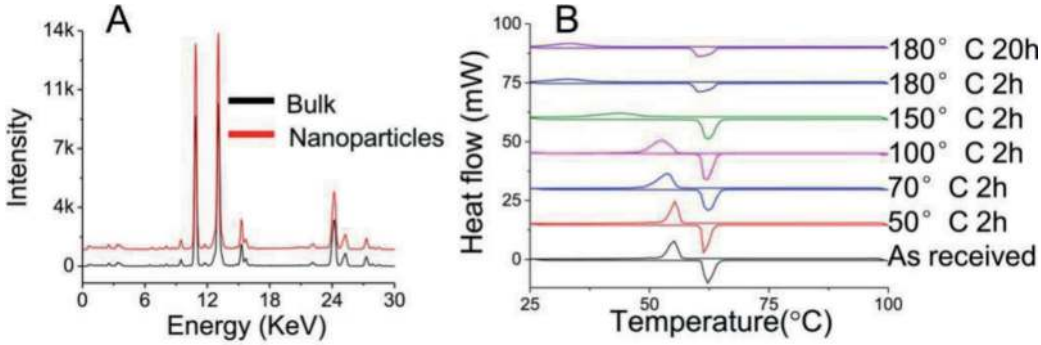

Figure 3.
X-ray fluorescence spectrum of bulk Field's alloy (black) and nanoparticles (red) (A); DSC curves of Field's alloy nanoparticles synthesized at different temperatures (50, 70, 100, 150, 180°C) for 2–20 h, respectively (B).

24.21, and 27.27 keV; $L_{\alpha 1}$ and $L_{\beta 1}$ of bismuth at 10.84 and 13.02 keV; and $K_{\alpha 1}$ of tin at 25.27 keV can be seen clearly. It indicated that no phase separation happens during the whole synthesis process.

DSC was used to measure the thermal properties of as-prepared nanoparticles. **Figure 3B** showed the DSC curves of bulk Field's alloy pellets and corresponding nanoparticles synthesized at different temperatures (50, 70, 100, 150, and 180°C) with other experimental conditions unchanged. For melting peaks of those samples, the peak position and shape were close and similar to the bulk material, where all of the samples are melt at about 62.5°C. However, for freezing peaks, it showed different characteristics for those nanoparticles synthesized at different temperatures. As the temperature increases, the freezing peak position would decrease and became more and more broaden. For example, the bulk Field's alloy was freezing at 55.2°C, and the nanoparticles synthesized at 50°C for 2 h, 70°C for 2 h, 100°C for 2 h, 150°C for 2 h, 180°C for 2 h, and 180°C for 20 h are at 55.2, 53.9, 52.5, 43.4, 32.6, and 32.6°C, respectively. Comparing the DSC curves of those samples under different temperatures, the reaction temperature-dependent freezing depressing was observed.

3.3 Thermal stability of Field's alloy nanoparticles and slurry

The thermal properties of Field's alloy slurry were investigated using a DSC. As shown in **Figure 4A**, the slurry can undergo melting-freezing phase transition during heating and cooling scanning processes. The downward endothermic peak at 62.5°C was belonging to the melting of the Field's alloy nanoparticles, while the upward

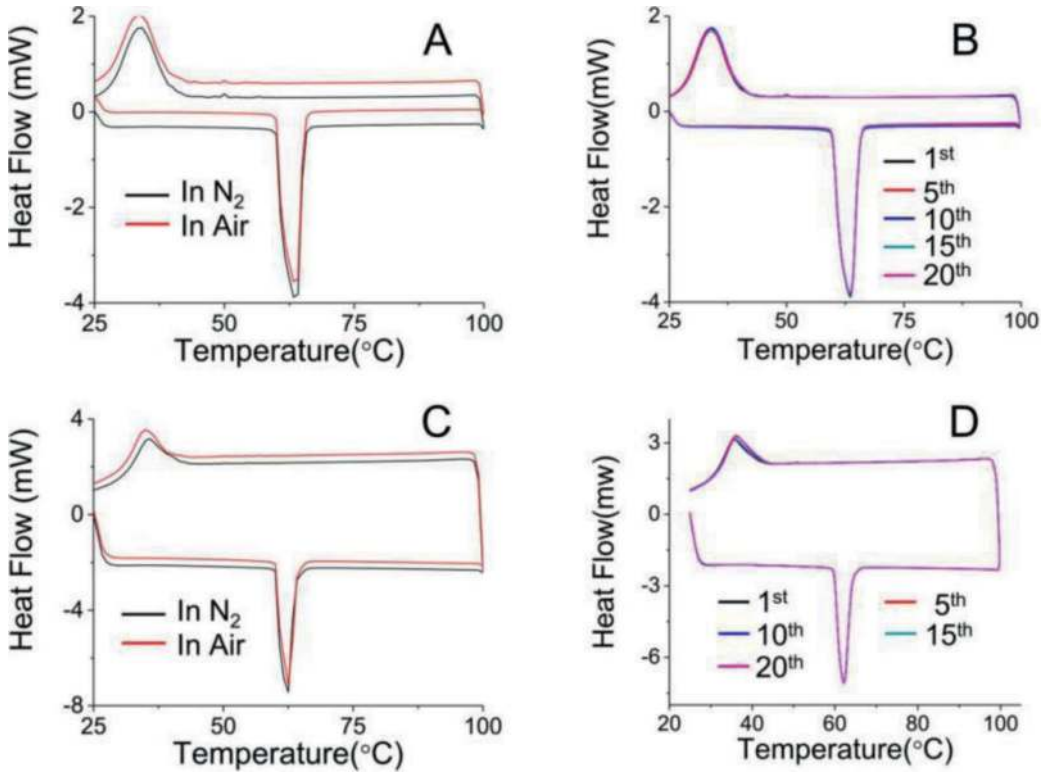

Figure 4.
Cyclic DSC curves of Field's alloy nanoparticles in ambient and nitrogen atmosphere, respectively (A); cyclic DSC curves of Field's nanoparticles after running in ambient condition for 1st, 5th, 10th, 15th, and 20th times, respectively (B); cyclic DSC curves of the slurry in ambient and nitrogen atmosphere (C); cyclic DSC curves of the slurry after running for 1st, 5th, 10th, 15th, and 20th times in ambient condition, respectively (D).

exothermic peak at 35.5°C was for their freezing. This observed melting-freezing temperature difference (about 27°C), called supercooling, had been well explained by the classical nucleation theory [39]. As shown in **Figure 4B**, no obvious changes of the slurry after running for 20 cycles, it suggested that slurry was very stable in ambient condition. It suggested that the nanoparticles are stable in ambient condition. As shown in **Figure 4C**, the nano-PCM slurry can undergo melting-freezing phase transition during heating and cooling scanning processes. The downward endothermic peak at 62.5°C was belonging to the melting of the Field's alloy nanoparticles, while the upward exothermic peak at 35.5°C was for their freezing. As shown in **Figure 4D**, no obvious changes of the nano-PCM slurry after running for 20 cycles, it suggested that nano-PCM slurry is very stable in the temperature range under 100°C.

4. Heat transfer loop test

In order to investigate the Field's alloy nanoparticle slurry compared to the pure liquid of HFE7100, a jet impingement heat transfer test was carried out. This part will represent some experimental data and discuss the effect of mass fraction of Field's alloy nanoparticle in slurry on pressure drop and heat transfer performance.

4.1 Experimental setup for heat transfer loop test

It is noted that all of the heat transfer loop tests were carried out under 1 atmospheric pressure. After installation of the heater, the test vessel was evacuated and filled with the working fluid, HFE7100. Additional degassing process was carried out by boiling the liquid pool for 2 hours to remove the dissolved noncondensibles. **Figure 5** illustrated the flow loop utilized to conduct the experiments. A variable

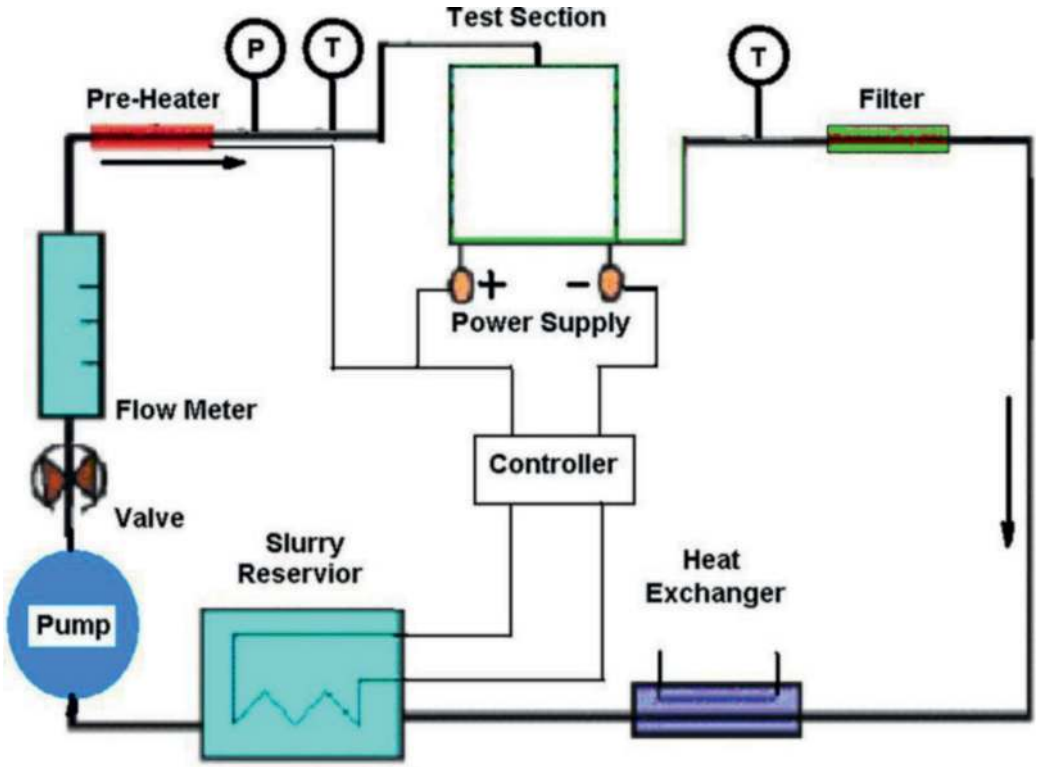

Figure 5.
Schematic diagram of the heat transfer loop test.

speed gear pump was used to supply coolant to the nozzle. A turbine flow meter was used to measure the volume flow rate. A vertically oriented nozzle was located directly above the heater surface. The distance between the nozzle exit and the test surface was fixed at 20 mm using a fine-threaded post-arrangement. The nozzle heater assembly was located in a chamber which also acts as the coolant reservoir.

4.2 Test chamber and heaters

Figure 6A illustrated the test chamber and **Figure 6B** showed our measured relationship between chamber pressure and saturation temperature of HFE7100.

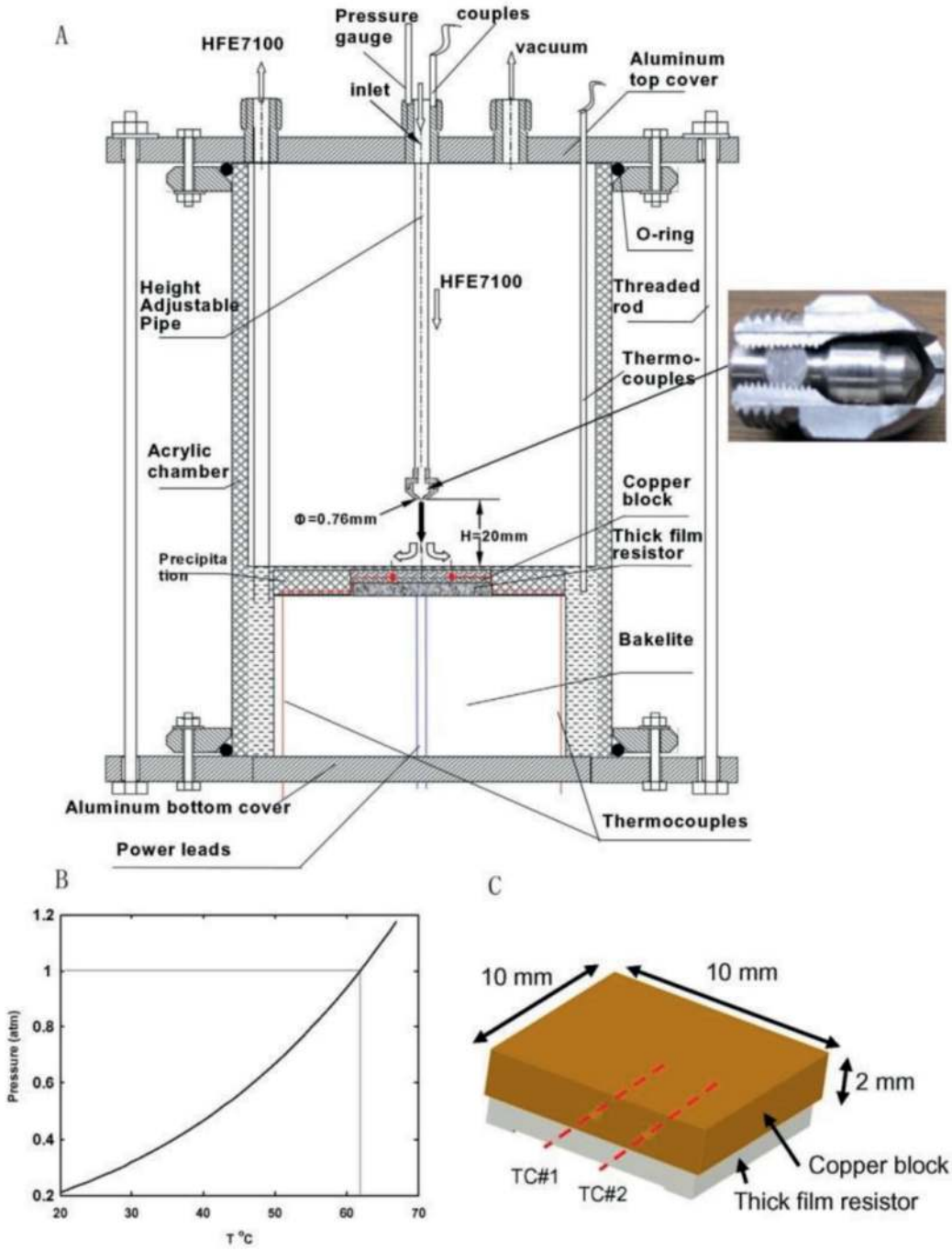

Figure 6.
Illustrated scheme of test chamber (A) temperature vs. pressure of HFE7100 (B) and heater (C).

The coolant within the reservoir was maintained at a constant temperature using a combination of an immersion heater and proper thermal insulation to ensure the test was under 1 atmosphere pressure. An acrylic cylinder with aluminum lids, which was 300 mm tall and 200 mm in diameter, was used as the test chamber. The test chamber contained approximately 500 ml of working slurry (pure HFE7100/ nano-PCM mixture). Heat was applied to the heater surface through a copper plate using a resistive heater controlled by a HP 6030A DC power supply system. The heater was built by soldering a 10×10×2-mm-copper block onto a matching size, 1-mm-thick resistive heater. **Figure 6C** showed the heater details. The resistive heater was made of a 5-ohm-thick film resistor with BeO substrate made by Barry Industries Inc. Soldering the thick film resistor to the copper plate minimizes the thermal contact resistance at the interface.

The temperature of slurry entering the test chamber was maintained at 56°C, 5°C below the liquid saturation temperature. Due to the large supercooling of nano-PCM particles (solidification temperature at 17.1°C), to ensure the PCM in solid phase, the slurry was chilled to 5°C by ice water. The nozzle inlet temperature (56°C) was controlled by an auxiliary heater powered by an AC regulator. The test heater surface was fastened at the bottom of the container using epoxy resin. The test vessel was insulated with a 25-mm-thick fiber glass blanket. A Bakelite layer (with a thermal conductivity less than 1 W/mK) underneath the heater was found to be a sufficient insulator. The uniformity of the Joule heating over the resistor surface was within 5%. The heat fluxes were also controlled at steady state for each set of testing. The jet impingement nozzle (a TG 0.7 full cone nozzle with the insert removed) was procured from Spraying Systems Co., and it had a passage with circular cross section, 0.76 mm in diameter. The coolant was allowed to enter the plenum of the nozzle where it flowed through a converging section as it existed to the chamber. Once the steady-state flow and temperature conditions were attained, the mean temperature of the heater and inlet and outlet temperatures of the slurry were calculated by the arithmetic mean of temperature readings. The heat transfer coefficient was then obtained by the following equation [40]:

$$h = Q/A(T_w - T_f) \quad (1)$$

where T_w is the average of the two surface temperatures extrapolated from the two embedded thermocouple readings. The pressure drop across the nozzle was measured at different mass fractions of slurry at a temperature of 20°C at the nozzle inlet (non-melting conditions).

4.3 Physical properties of Field's alloy nanoparticle slurry in HFE7100

For the silane monolayer modified Field's alloy nanoparticles, the optical transmittance of nanoparticle suspensions in HFE7100 fluid was monitored by a portable spectrometer, and the optical transmittance kept nearly the same over 1 month, which indicates the nanoparticle suspension is highly stable for more than a month after the 1H, 1H, 2H, 2H-perfluorooctyltriethoxysilane modification. The physical properties of nano-PCM slurry in HFE7100 with 10, 23, and 30% particle mass fraction, where the corresponding particle volume fractions of slurry are 2.3, 6.4, and 8.0%, and its components are presented in **Table** 1. The bulk viscosity of Field's alloy nanoparticle slurry is measured by using a calibrated Cannon-Fenske viscometer. Other parameters, such as density, thermal conductivity, and latent heat of Field's alloy nano-PCM slurry, are calculated according to the reference data and mixture equations [41]. The specific heat of nanoparticles for solid/liquid phases is derived from the superposition calculations involving HFE7100 and Field's alloy (solid/liquid).

Slurry and its components	Density (kg m^{-3})	Specific heat (J $kg^{-1}K^{-1}$)	Thermal conductivity (W $m^{-1}K^{-1}$)	Latent heat (kJ kg^{-1})	Viscosity (mPa s) at 293 K
Field's alloy[a] (solid)	7880	170.5	70.1	40.2	–
Field's alloy (liquid)	7880	170.5	34.5	–	–
HFE7100 (298 K)[b]	1500	1180	0.07	–	0.60
Slurry[c] 10%	1648	1079	0.075	4	0.69
23%	1883	948	0.084	9	0.75
30%	2036	877	0.091	11	0.79

[a] *http://www.Matweb.com [42].*

[b] *3M Data Book, HFE7100 for Heat Transfer, 2002 [43].*

[c] *Bulk physical properties of slurries are calculated from those of solid PCM particles.*

Table 1.
Physical properties of Field's alloy nano-PCM slurry and its components.

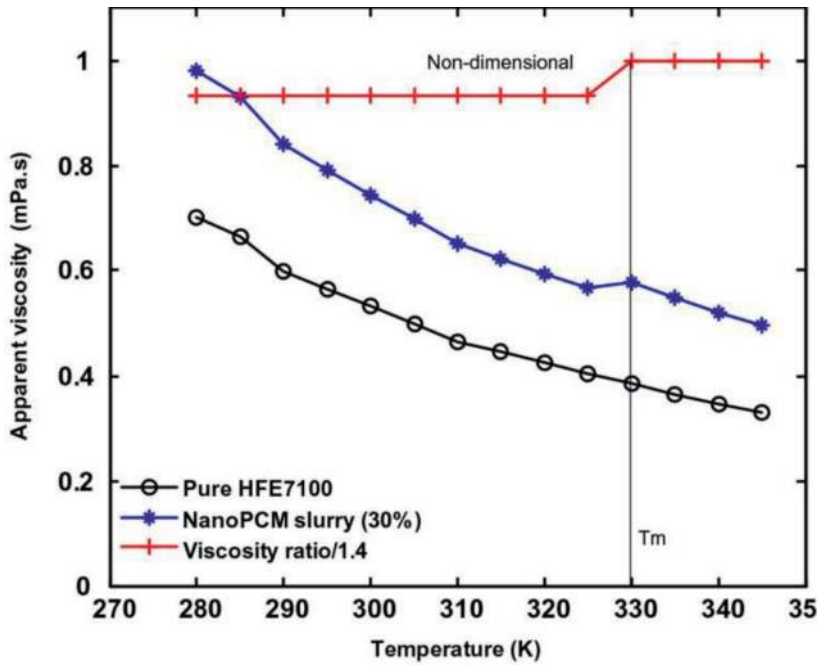

Figure 7.
Effect of temperature on apparent viscosity of pure HFE7100 and nano-PCM slurry.

A relation exists between the temperature of HFE7100 with Field's alloy nanoparticles slurry and its apparent viscosity. **Figure 7** shows the measured experimental data that exhibits the effect of temperature on apparent viscosity of pure HFE7100 and slurry with 30% (wt%) particle fraction. The results show that the ratio of the slurry viscosities keeps almost the same at 1.4 over the tested temperature range.

4.4 Pressure drop

An important parameter was pressure drop between the inlet and the outlet of microchannel heat exchanger. In ideal case, the pressure drop should be as small

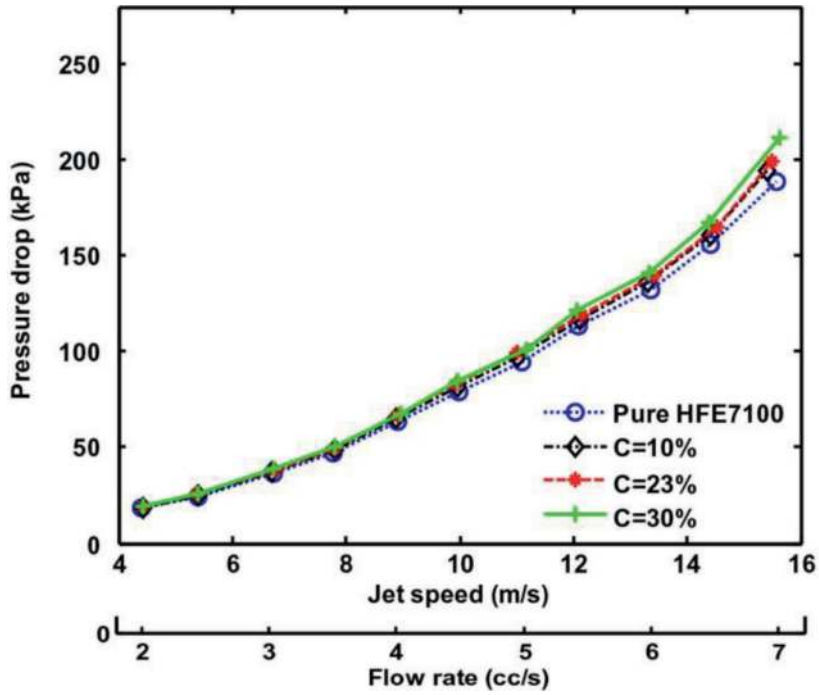

Figure 8.
Jet impingement pressure drop data with different Field's nanoparticle concentrations (nozzle: TG0.76, H = 20 mm); the inlet temperature is controlled at 20°C.

as possible to minimize pumping power. When the velocity of the jet was varied between 4.2 and 15.5 m/s, the pressure drop across the nozzle was measured at flow rates of 1.95–7.15 cc/s. As shown in **Figure 8**, when the nozzle inlet temperature of the liquid temperature was controlled at 20°C, the jet impingement pressure drop results were very close even with different particle mass fractions. It can be assigned to the comparable increases in Field's alloy nanoparticle slurry viscosity and density with increased nanoparticle mass fraction (see **Table** 1). The pressure drop was related to the nozzle Reynolds number as $\triangle P \propto Re_d^{-0.25}$ [44]. Since the nozzle Reynolds number did not change too much with increased particle mass fraction, the pressure drop should not vary significantly with particle mass concentration.

4.5 Heat transfer performance of Field's alloy nanoparticle slurry

Heat transfer performance of the nanoparticle slurries was evaluated by measuring their convective heat transfer coefficients in jet impingement configuration. When no solid-liquid and liquid-vapor phase change occurs in the slurry, the jet impingement heat transfer coefficient can be predicted by the Martin correlation [45]. **Figure 9** showed the heat transfer coefficient of jet impingement test for pure HFE7100 when the inlet nozzle temperature was kept at 20°C with a flow rate from 2.05 to 6.95 cc/s. When the flow rate was from 2.05 to 6.95 cc/s, the heat transfer coefficient was increased from 4.6 to 9.4 103 W/m^2 K. The difference between the experimental data and the Martin correlation was within 10% of the Martin correlation.

In order to compare the heat transfer performance between HFE7100 and the slurries with different particle mass fractions, the flow rate constant was set at 7.15 cc/s, and the temperature of the liquids at the nozzle inlet was fixed at 56°C. The heater surface temperature was varied between 56 and 75°C by controlling the heater power input. The comparison for the overall performance of pure HFE7100 (0%) and slurries with 10, 23, and 30% particle mass fraction, using heat flux as a measure, was provided in **Figure 10**. It can be seen that even before the melting temperature of

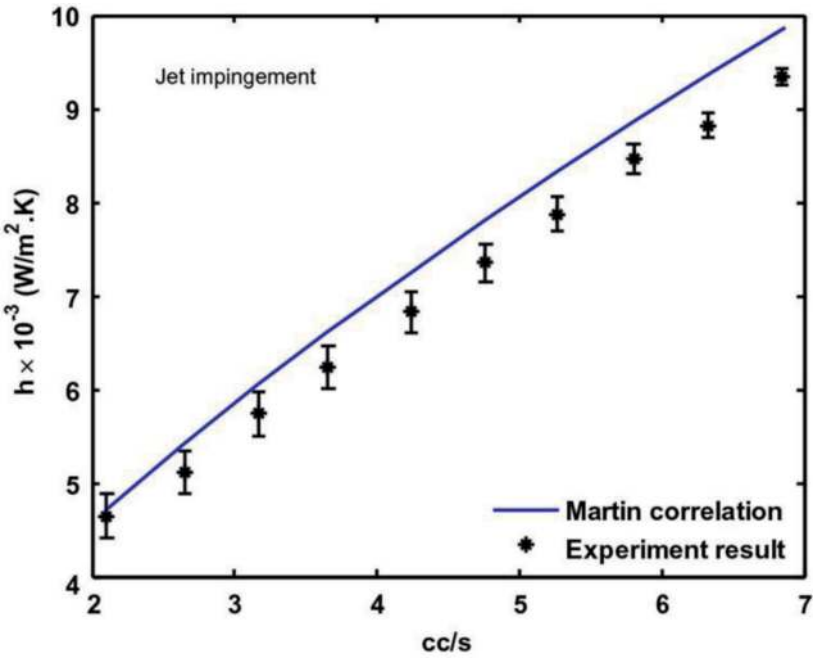

Figure 9.
Experimental and Martin correlation of heat transfer coefficients of pure HFE7100 when the inlet temperature is 20°C.

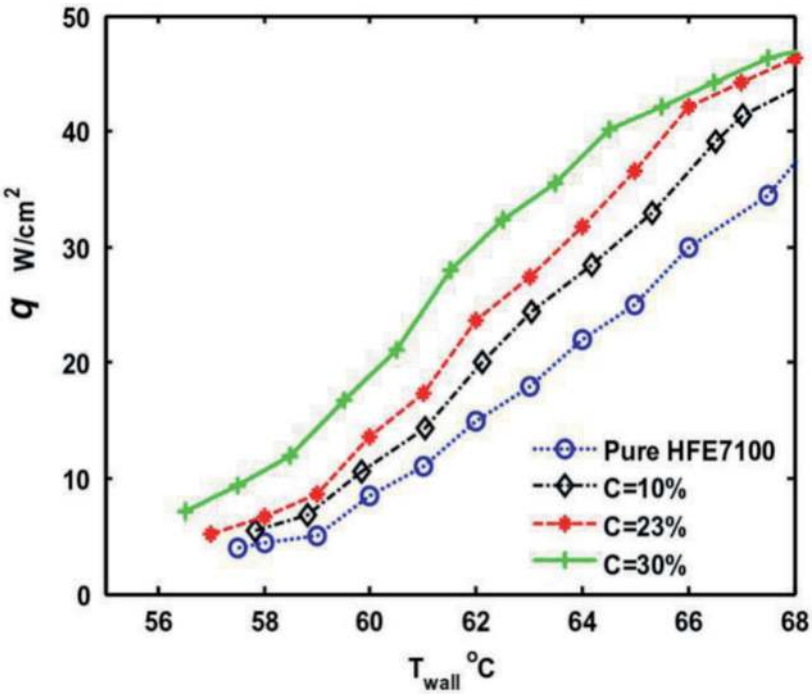

Figure 10.
HFE7100 jet impingement (56–68°C) heat flux at the flow rate of 7.15 cc/s; (note: the inlet T_{in} was controlled at 56°C, nozzle: TG0.76, H = 20 mm). Slurry with 30% particle mass fraction improved average heat transfer coefficient by 70% when compared to pure HFE7100 for jet impingement at the temperature range from 62 to 66°C.

Field's alloy and the boiling point of HFE7100 were reached, the slurries had a higher heat flux at surface temperature between 56 and 60°C. This can be attributed, in part to their higher thermal conductivity. At the heater surface of 62°C, the results clearly

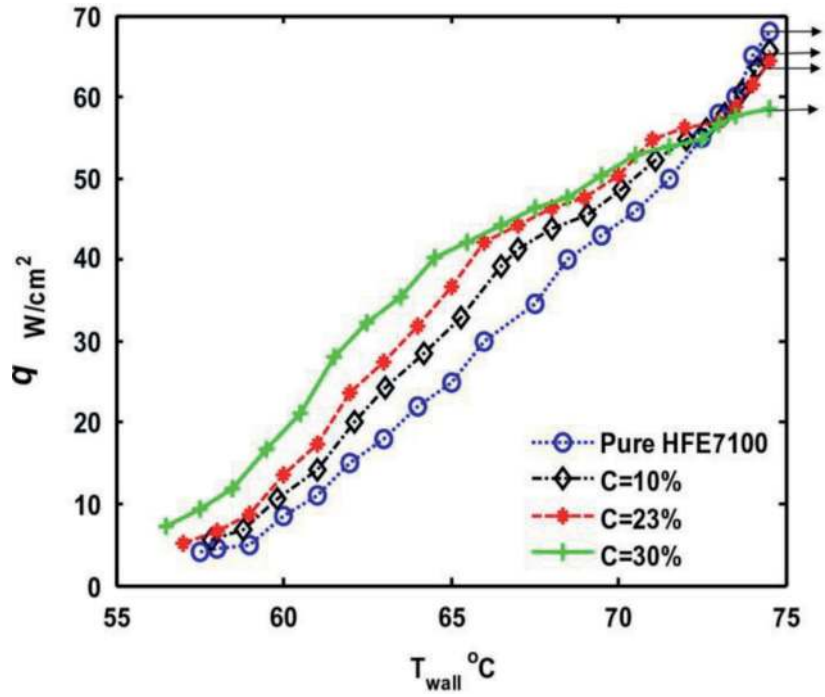

Figure 11.
Heater surface temperature at full range (56–75°C) at the flow rate of 7.15 cc/s; (note: the inlet T_{in} was controlled at 56°C, nozzle: TG0.76, H = 20 mm), black arrow was the critical heat flux.

indicated that the slurry with 30% particle mass fraction provides a much higher heat flux than pure HFE7100. The heat flux removal increased from 15 to 30 W/cm^2, a 100% improvement. At 64°C, the results showed that the slurry with 30% particle mass fraction increases heat flux from 22 to 38 W/cm^2, a 73% improvement. The results also show that at 66°C, the slurry with 30% particle mass fraction had a higher heat flux, 30 W/cm^2 vs. 44 W/cm^2, a 47% improvement. On the average, the slurry with 30% particle mass fraction provided a heat transfer enhancement of 70% when compared to pure HFE7100.

It was noted that the heat transfer enhancement was heat-flux dependent. It begun to decrease as the heat flux increased because of the increasingly higher temperature difference between the wall and the slurry. High heat flux can shift the slurry temperature out of the melting range (>62°C). **Figure 11** showed the heat removal results at a flow rate of 7.15 cc/s over a wider surface temperature range, between 56 and 75°C. It was interesting to note that, at surface temperature higher than 73°C, the critical heat flux decreased as the particle fraction increased from 10 to 30%. This could be explained by the increase in viscosity and latent heat of melting depletion. These combined effects could reduce the overall heat removal capability of nano-PCM slurry. At a surface temperature of 75°C and flow rate of 7.15 cc/s, the heat fluxes of the slurry with 30% particle mass fraction and that of pure HFE7100 were 59 and 69 W/cm^2, respectively. **Figure 12** showed the heat transfer coefficients of slurries with several particle mass fractions vs. the heater surface temperature at a flow rate of 7.15 cc/s. The figure showed the heat transfer coefficients of nano-PCM slurries peak at 60–63°C.

The reported heat transfer results in **Figures 10–12** were the average values from three consecutive repeated tests. Depending on the temperature of the heater, a heat loss of 4.5% of the electrical power input was estimated by calibration. The heat flux at the surface of the copper plate was obtained from the measured electrical power. Data in **Figures 10** and **11** were the heat transfer coefficients from five consecutive tests after accounting for the heat loss. All experiments had random

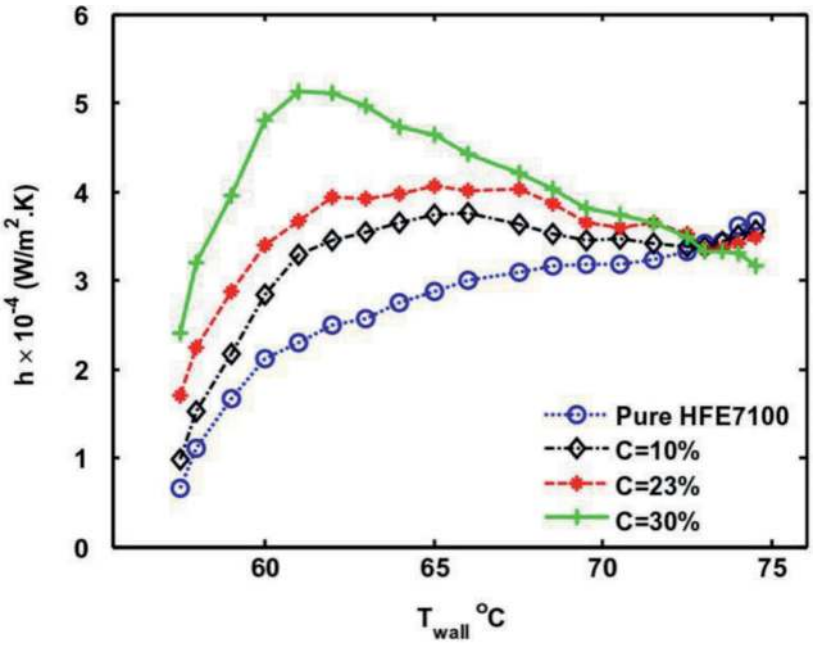

Figure 12.
Heat transfer coefficients of slurry with 30% particle mass fraction vs. heater surface temperature of full range (56–75°C) at the flow rate of 7.15 cc/s (note: the inlet T_{in} was controlled at 56°C, nozzle: TG0.76, H = 20 mm).

errors which occurred inevitably during measurements. These errors may be analyzed with the calculation of the root-mean-square of errors (RMSE) defined as RMSE = $\sqrt{\frac{1}{n}\left(\Sigma_1^n\left(\frac{h - h_{exp}}{h}\right)\right)}$ where n was the size of the sample (n = 5). The RMSE values for pure HFE7100, 10% slurry, 23% slurry, and 30% slurry are 0.013, 0.036, 0.04, and 0.049, respectively. During these measurements the maximum root-mean-square of errors (RMSE) was found to be less than 5% representing a reasonable degree of accuracy.

Our data from the slurries with nano-PCMs demonstrated very consistent thermal performance. The 30% nano-PCM slurry attains 97% of its initial heat transfer performance after 5000 thermal cycles. This implied that encapsulation of the nano-PCM particles with a shell made of materials such as silica, normally used to prevent coalescence of molten nanoparticles, was not needed for the slurry featuring HFE7100 and Field's alloy nano-PCM. The main reason was thought to be the existence of oxide shells around the nanoparticles. Oxidation of Field's alloy was unavoidable during the synthesis process and can provide a thin protective shell for the core material for a long time. Furthermore, two other possible mechanisms might be helping the bare nano-PCMs. First, the added perfluorooctyltriethoxysilane surfactant helped resist coalescence of molten Field's alloy nanoparticles and ensured the stability of colloidal suspension. Second, bare Field's alloy nanoparticles had residual charges which generate repulsive electrical force to prevent the agglomeration of molten nanoparticles.

5. Conclusions

In this chapter, a facile one-step method was developed for the production of Field's alloy nanoparticles or slurry using nanoemulsification technique. The composition, size, morphology, and thermal properties of as-prepared nanoparticles were characterized by XRF, TEM, and DSC, respectively. The slurry with modified Field's alloy nanoparticle dispersed in PAO or HFE7100 exhibits good thermal

properties and stability, which showed promising potential applications in cooling of electronic device, engines, and other systems. Meanwhile, an experimental study was performed to investigate jet impingement heat transfer of Field's alloy nanoparticles-HFE7100 slurry. The Field's alloy nano-PCM absorbed heat during a phase change process from solid to liquid phase coupled with HFE7100 evaporation process. The study showed that the mass fraction of nanoparticles played an insignificant role in pressure drop but an important role on heat transfer performance. The high heat flux removal capability had been demonstrated by repeated closed loop test. Away from the critical heat flux, Field's alloy nano-PCM slurry provided a significant heat transfer enhancement due to the increase in the thermal capacity of the carrier fluid. Moreover, the nano-PCM slurries were able to maintain 97% of their heat removal capability after 5000 thermal cycles.

Acknowledgements

This work is supported by the by the National Natural Science Foundation of China (Grant No. 51672227) and the Fundamental Research Funds for the Central Universities (Grant No. YX2682015RC08, 2682017CY08 and 2682017CX089).

Conflict of interest

The authors declare no conflict of interest.

Nomenclature

A	area of the heat transfer (m^2)
c_p	heat capacity of the working fluid (J/kg K)
k	thermal conductivity of working fluid (W/m K)
h_{sl}	latent heat of the Field's alloy (J/kg)
h	heat transfer coefficient of jet impingement or spray (W/m^2 K)
Q	total power (W)
q	heat flux (W/m^2)
R	thermal resistance (K/W)
r	radius (m)
T	temperature (K)
T_f	temperature of inlet fluid (K)
ϕ	volume fraction of nanoparticles in the working fluid
Greeks	
q	density (kg/m^3)
s	melting time (s)
l	viscosity (Pa s)
Subscripts	
b	bulk
d	diameter of nozzle
f	carrier fluid
l	melted Field's alloy
m	melting
p	particle
w	wall
s	solid

Author details

Chaoming Wang[1,2*], Xinran Zhang[1], Wenbing Jia[2], Wei Wu[3] and Louis Chow[3]

1 Applied Mechanics and Structure Safety Key Laboratory of Sichuan Province, School of Mechanics and Engineering, Southwest Jiaotong University, Chengdu, China

2 Key Laboratory for Advanced Technologies of Materials, Ministry of Education, School of Materials Science and Engineering, Southwest Jiaotong University, Chengdu, China

3 Department of Mechanical and Aerospace Engineering, University of Central Florida, Orlando, FL, USA

*Address all correspondence to: hbdxwcm@hotmail.com

IntechOpen

References

[1] Kurtcebe C, Erim MZ. Heat transfer of a non-Newtonian viscoinelastic fluid in an axisymmetric channel with a porous wall for turbine cooling application. International Communications in Heat and Mass Transfer. 2002;**29**:971-982

[2] Liu M, Bruno F, Saman W. Thermal performance analysis of a flat slab phase change thermal storage unit with liquid-based heat transfer fluid for cooling applications. Solar Energy. 2011;**85**:3017-3027

[3] Forgber T, Radl S. Heat transfer rates in wall bounded shear flows near the jamming point accompanied by fluid-particle heat exchange. Powder Technology. 2017;**315**:182-193

[4] Hryniewicz P, Szeri AZ, Jahanmir S. Application of lubrication theory to fluid flow in grinding: Part I—Flow between smooth surfaces. Journal of Tribology-Transactions of the ASME. 2001;**123**:94-100

[5] Kim E. The influence of Reynolds number and heat transfer in fluid film lubrication. Mechanics Research Communications. 1996;**23**:441-448

[6] Wannapakhe S, Rittidech S, Bubphachot B, Watanabe O. Heat transfer rate of a closed-loop oscillating heat pipe with check valves using silver nanofluid as working fluid. Journal of Mechanical Science and Technology. 2009;**23**:1576-1582

[7] Navas J, Sanchez-Coronilla A, Martin EI, Teruel M, Gallardo JJ, Aguilar T, et al. On the enhancement of heat transfer fluid for concentrating solar power using Cu and Ni nanofluids: An experimental and molecular dynamics study. Nano Energy. 2016;**27**:213-224

[8] Yang JC, Li FC, He YR, Huang YM, Jiang BC. Experimental study on the characteristics of heat transfer and flow resistance in turbulent pipe flows of viscoelastic-fluid-based Cu nanofluid. International Journal of Heat and Mass Transfer. 2013;**62**:303-313

[9] Modak M, Sharma AK, Sahu SK. An experimental investigation on heat transfer enhancement in circular jet impingement on hot surfaces by using Al_2O_3/water nano-fluids and aqueous high-alcohol surfactant solution. Experimental Heat Transfer. 2018;**31**:275-296

[10] Rajendran DR, Sundaram EG, Jawahar P. Experimental studies on the thermal performance of a parabolic dish solar receiver with the heat transfer fluids SiC plus water nano fluid and water. Journal of Thermal Science. 2017;**26**:263-272

[11] Asadi A, Asadi M, Rezaniakolaei A, Rosendahl LA, Afrand M, Wongwises S. Heat transfer efficiency of Al_2O_3-MWCNT/thermal oil hybrid nanofluid as a cooling fluid in thermal and energy management applications: An experimental and theoretical investigation. International Journal of Heat and Mass Transfer. 2018;**117**:474-486

[12] Pal R. A novel method to determine the thermal conductivity of interfacial layers surrounding the nanoparticles of a nanofluid. Nanomaterials. 2014;**4**:844-855

[13] Song SH, Shen WD, Wang JL, Wang SC, Xu JF. Experimental study on laminar convective heat transfer of microencapsulated phase change material slurry using liquid metal with low melting point as carrying fluid. International Journal of Heat and Mass Transfer. 2014;**73**:21-28

[14] Tao YB, You Y, He YL. Lattice Boltzmann simulation on phase change heat transfer in metal foams/

paraffin composite phase change material. Applied Thermal Engineering. 2016;**93**:476-485

[15] Liu YS, Yang YZ. Preparation and thermal properties of $Na_2CO_3{\cdot}10H_2O$-$Na_2HPO_4{\cdot}12H_2O$ eutectic hydrate salt as a novel phase change material for energy storage. Applied Thermal Engineering. 2017;**112**:606-609

[16] Kahwaji S, Johnson MB, Kheirabadi AC, Groulx D, White MA. Fatty acids and related phase change materials for reliable thermal energy storage at moderate temperatures. Solar Energy Materials & Solar Cells. 2017;**167**:109-120

[17] Aydin AA, Aydin A. High-chain fatty acid esters of 1-hexadecanol for low temperature thermal energy storage with phase change materials. Solar Energy Materials & Solar Cells. 2012;**96**:93-100

[18] Deng YY, Yang LJ. Preparation and characterization of polyethylene glycol (PEG) hydrogel as shape-stabilized phase change material. Applied Thermal Engineering. 2017;**114**:1014-1017

[19] Lv PZ, Liu CZ, Rao ZH. Experiment study on the thermal properties of paraffin/kaolin thermal energy storage form-stable phase change materials. Applied Energy. 2016;**182**:475-487

[20] Chen Z, Feng S, Cao L, Fang G. Synthesis and thermal properties of shape-stabilized lauric acid/activated carbon composites as phase change materials for thermal energy storage. Solar Energy Materials & Solar Cells. 2012;**102**:131-136

[21] Han ZH, Cao FY, Yang B. Synthesis and thermal characterization of phase-changeable indium/polyalphaolefin nanofluids. Applied Physics Letters. 2008;**92**:2252

[22] Ma Y, Chu X, Tang G, Yao Y. Synthesis and thermal properties of acrylate-based polymer shell microcapsules with binary core as phase change materials. Materials Letters. 2013;**91**:133-135

[23] Hong Y, Ding S, Wu W, Hu J, Voevodin AA, Gschwender L, et al. Enhancing heat capacity of colloidal suspension using nanoscale encapsulated phase-change materials for heat transfer. ACS Applied Materials & Interfaces. 2010;**2**:1685-1691

[24] Wang Y, Xia Y. Bottom-up and top-down approaches to the synthesis of monodispersed spherical colloids of low melting-point metals. Nano Letters. 2004;**4**:2047-2050

[25] Fang Y, Kuang S, Gao X, Zhang Z. Preparation and characterization of novel nanoencapsulated phase change materials. Energy Conversion and Management. 2008;**49**:3704-3707

[26] Tiarks F, Landfester K, Antonietti M. Preparation of polymeric nanocapsules by miniemulsion polymerization. Langmuir. 2001;**17**:908-918

[27] Canter N. Heat transfer fluid based on nanoparticles dispersed in ionic liquids. Tribology and Lubrication Technology. 2014;**70**:10-11

[28] Manikandan S, Rajan KS. New hybrid nanofluid containing encapsulated paraffin wax and sand nanoparticles in propylene glycol-water mixture: Potential heat transfer fluid for energy management. Energy Conversion and Management. 2017;**137**:74-85

[29] Krishnamurthy MR, Kumar G, Gireesha BJ, Rudraswamy NG. MHD flow and heat transfer (PST and PHF) of dusty fluid suspended with alumina nanoparticles over a stretching sheet embedded in a porous medium under the influence of thermal radiation. Journal of Nanofluids. 2018;**7**:527-535

[30] Vu T, Tran TN, Xu JJ. Single-phase flow and heat transfer characteristics of ethanol/polyalphaolefin nanoemulsion fluids in circular minichannels. International Journal of Heat and Mass Transfer. 2017;**113**:324-331

[31] Yu LY, Liu D, Botz F. Laminar convective heat transfer of alumina-polyalphaolefin nanofluids containing spherical and non-spherical nanoparticles. Experimental Thermal and Fluid Science. 2012;**37**:72-83

[32] Wang X, Niu J, Li Y, Wang X, Chen B, Zeng R, et al. Flow and heat transfer behaviors of phase change material slurries in a horizontal circular tube. International Journal of Heat and Mass Transfer. 2007;**50**:2480-2491

[33] Yamagishi Y, Takeuchi H, Pyatenko AT, Kayukawa N. Characteristics of microencapsulated PCM slurry as a heat-transfer fluid. AICHE Journal. 2010;**45**:696-707

[34] Zeng R, Wang X, Chen B, Zhang Y, Niu J, Wang X, et al. Heat transfer characteristics of microencapsulated phase change material slurry in laminar flow under constant heat flux. Applied Energy. 2009;**86**:2661-2670

[35] Nan CW, Birringer R, Clarke DR, Gleiter H. Effective thermal conductivity of particulate composites with interfacial thermal resistance. Journal of Applied Physics. 1997;**81**:6692-6699

[36] Hu X, Zhang Y. Novel insight and numerical analysis of convective heat transfer enhancement with microencapsulated phase change material slurries: Laminar flow in a circular tube with constant heat flux. International Journal of Heat and Mass Transfer. 2002;**45**:3163-3172

[37] Wang C, Zhang X, Su M. Synthesis and thermal stability of Field's alloy nanoparticles and nanofluid. Materials Letters. 2017;**205**:6-9

[38] Wu W, Chow LC, Wang CM, Su M, Kizito JP. Jet impingement heat transfer using a Field's alloy nanoparticle – HFE7100 slurry. International Journal of Heat and Mass Transfer. 2014;**68**:357-365

[39] Vehkamaki H. Classical Nucleation Theory in Multicomponent Systems. New York: Springer; 2006

[40] Incropera FP, Dewitt DP. Introduction to Heat Transfer. John Wiley & Sons; 2006

[41] Maxwell JC. A Treatise on Electricity and Magnetism. New York: Dover; 1954

[42] Kizilkan O, Dincer I. Borehole thermal energy storage system for heating applications: Thermodynamic performance assessment. Energy Conversion and Management. 2015;**90**:53-61

[43] Miro L, Oro E, Boer D, Cabeza LF. Embodied energy in thermal energy storage (TES) systems for high temperature applications. Applied Energy. 2015;**137**:793-799

[44] Fox RW, McDonald A. Introduction to Fluid Mechanics. New Jersey: John Wiley & Sons; 2011

[45] Martin H. Advances in Heat Transfer. Vol. 13. New York: Academic Press; 1977